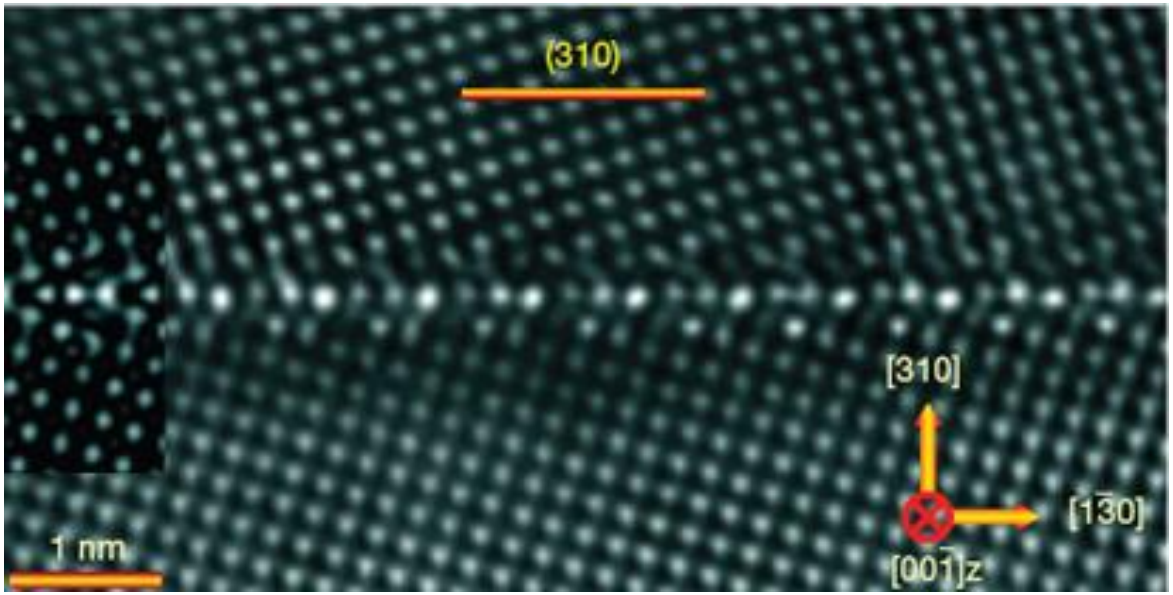

Изображение межзеренной границы в MgO, полученное методом спектроскопии характеристических потерь энергии электронами (EELS).

Z.Wang et al., Atom-resolved imaging of ordered defect superstructures at individual grain boundaries. Nature 479, 380 (2011).

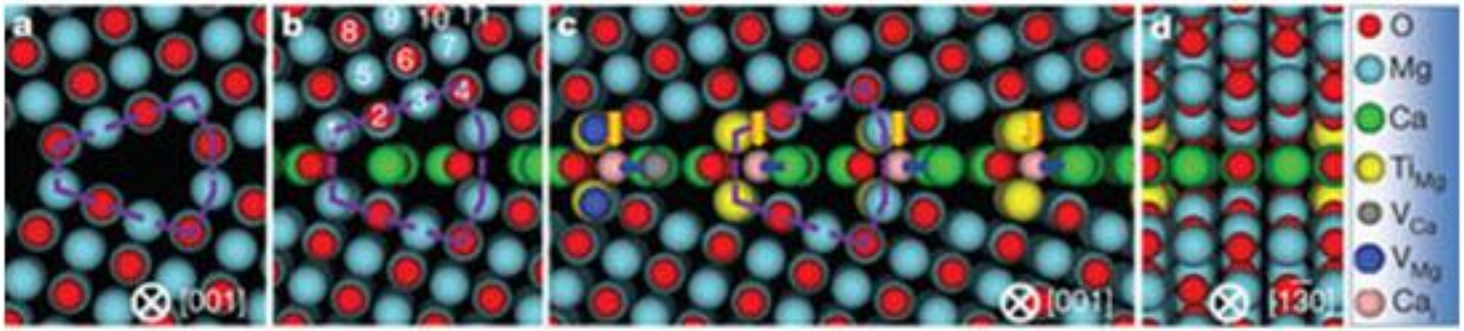

Модель межзеренной границы в MgO: сверхячейка чистой границы, обозначенная пунктирным контуром (a), сверхячейка с сегрегированным кальцием (b), модель границы по направлению [001] (c) и [1-30] (d), стрелками показано смещение кальция в сверхячейке.

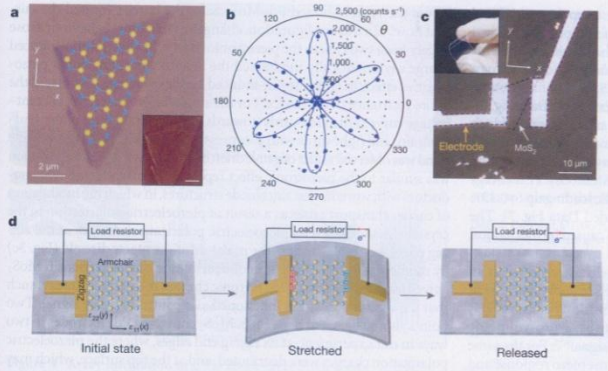

Figure 1 | Single-layer MoS_2 piezoelectric device and operation scheme. **a**, Optical image of the single-atomic layer MoS_2 flake with superimposed lattice orientation derived from SHG results. Blue and yellow spheres represent Mo and S atoms, respectively. Inset: atomic force microscopy image of the flake. Scale bar 2 μm. **b**, Polar plot of the SH intensity from single-layer MoS_2 as a function of the crystal's azimuthal angle θ. The symbols are experimental data and the solid lines are fits to the symmetry analysis described in the text. **c**, A typical flexible device with single-layer MoS_2 flake and electrodes at its zigzag edges. Inset: optical image of the flexible device. **d**, Operation scheme of the single-layer MoS_2 piezoelectric device. When the device is stretched, piezoelectric polarization charges of opposite polarity (plus and minus symbols) are induced at the zigzag edges of the MoS_2 flake. Periodic stretching and releasing of the substrate can generate piezoelectric outputs in external circuits with alternating polarity (as indicated by the red arrows).

strain: for single-layer MoS_2 with width of ~5 μm and a length of ~10 μm, the peak open-circuit voltage reached 18 mV and the peak short-circuit current reached 27 pA (Fig. 2b), with voltage and current responsivities of 55.1 ± 12.3 pA and 32.8 ± 4.5 mV, respectively, for each 1% change in strain. There were no significant electrical outputs from bare PET substrates without a single-layer MoS_2 flake (Extended Data Fig. 5b).

The dependence of piezoelectric charge polarization on the directions of principal strain in 2D materials was also investigated. The coupling between polarization (P_i) and strain (ε_{jk}) tensor can be quantified to first order by the third-rank piezoelectric tensor $e_{ijk} = (\partial P_i / \partial \varepsilon_{jk})$, where $i, j, k \in (1, 2, 3)$, with 1, 2 and 3 corresponding to the x, y and z axes, respectively. Symmetry analysis of the D_{3h} point group suggested that there was only one non-zero independent coefficient e_{11} for single-layer MoS_2. The in-plane polarization along the x axis, sensed by the metal electrodes as shown in Fig. 1d, can be expressed as $P_1 = e_{11}(\varepsilon_{11}\text{-}\varepsilon_{22})$, whereas P_2 along the y axis is related to the pure shear strain ε_{12} and can be ignored in these experiments. A distinctive consequence of this symmetry is that the output is expected to reverse sign when the strain is rotated from the x ('armchair') to the y ('zigzag') direction. This was verified experimentally, as shown in the bottom panel of Fig. 2a.

To quantify the power output of the piezoelectric circuit, it is necessary to study the voltage and current outputs as a function of load resistance, as shown in Fig. 2c (see Extended Data Fig. 6 for circuit details). The

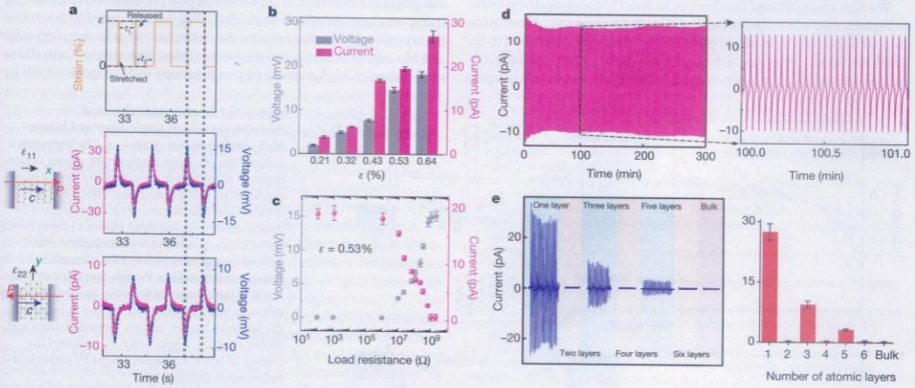

Figure 2 | Piezoelectric outputs from single-layer and multi-layer MoS_2 devices. **a**, Voltage response with 1 GΩ external load and short-circuit current response of a single-layer MoS_2 device under periodic strain in two different principal directions. Top: applied strain as a function of time. Middle: corresponding piezoelectric outputs from single-atomic-layer MoS_2 when strain is applied in the x direction (armchair direction). Bottom: corresponding piezoelectric outputs from the same device when strain is applied in the y direction (zigzag direction). The phase difference highlighted by black dashed lines is obtained by theoretical derivation and has been intentionally exaggerated for clarity, not experimental measurement. Red, blue and black arrows represent the directions of polarization, the polar axis of MoS_2 and principal strains, respectively. **b**, Dependence of piezoelectric outputs from a single-layer MoS_2 device on the magnitude of the applied strain. Mean values from 20 technical replicates are indicated. Error bars represent s.d. **c**, Dependence of voltage and current outputs from a single-layer MoS_2 device under 0.53% strain as a function of load resistance. Mean values from 20 technical replicates are indicated. Error bars represent s.d. **d**, Cyclic test showing the stability of single-layer MoS_2 device for prolonged period. **e**, Evolution of the piezoelectric outputs with increasing number of atomic layers (n) in MoS_2 flakes. For each device, mean values from 20 technical replicates are indicated. Error bars represent s.d.

Пьезоэлектрический эффект в моноатомном (двумерном) MoS_2.

Wenzhuo Wu, et. al. Piezoelectricity of single-atomic-layer MoS_2 for energy conversion and piezotronics. Nature. 2014. v. 514. 471-474.

Асимметричная модуляция переноса зарядов в двумерном материале (пьезотронный эффект).

drain electrode. The metal–semiconductor–metal (MSM) device as fabricated consisted of two back-to-back Schottky barriers, and transport and Mo-edge at the drain and source electrodes, respectively. Controllable modulation of M–S contacts or *p*–*n* junctions in 2D nanomaterials by

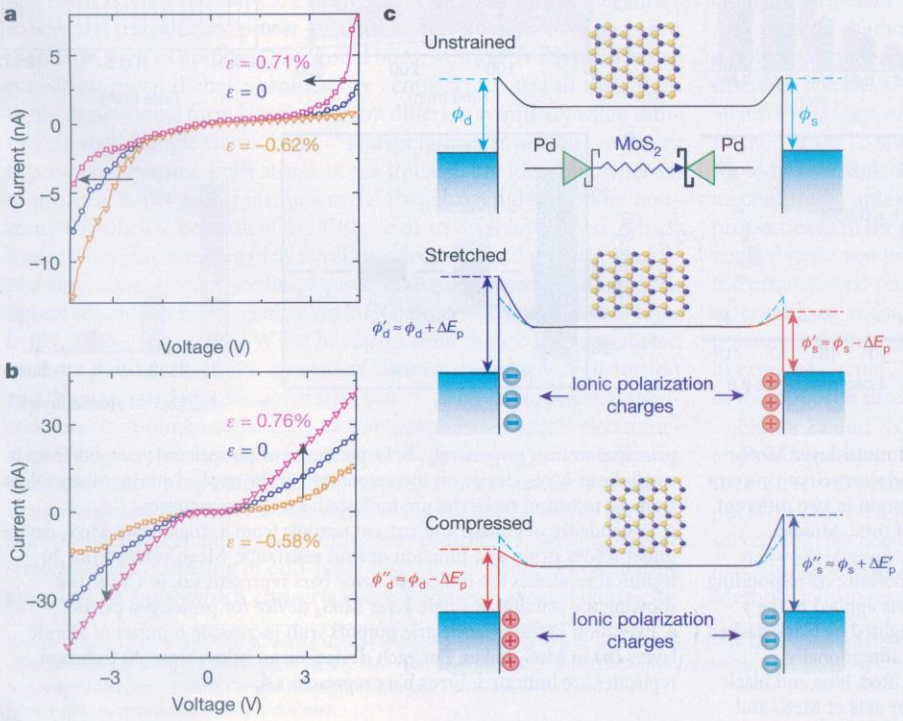

Figure 3 | Direct-current electrical characterizations of single-layer and bilayer MoS_2 devices under strains. **a**, The asymmetric modulation of carrier transport by strains under opposite drain bias in a single-layer device shows characteristics of a piezotronic effect. **b**, The symmetrical modulation of carrier transport by strains under opposite drain bias in a bilayer device shows characteristics of a piezoresistive effect. **c**, Band diagrams explaining the piezotronic behaviour observed in a single-layer device as a result of the changes in Schottky barrier heights by strain-induced polarization. ϕ_d and ϕ_s represent the Schottky barrier heights formed at drain and source contacts, respectively. E_p indicates the change in Schottky barrier height by piezoelectric polarization charges.

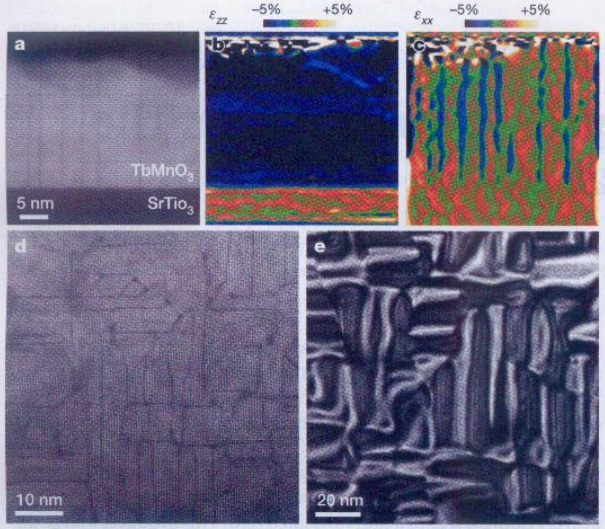

Figure 1 | Atomic-resolution domain structure of strained $TbMnO_3$. **a**, Cross-sectional HAADF-STEM image of a 25 nm-thick $TbMnO_3$ thin film grown on $SrTiO_3$. **b**, **c**, Components ε_{zz} (**b**) and ε_{xx} (**c**) of the strain tensor (colour scales), obtained by geometrical phase analysis of **a**. This shows that the domains grow uniformly strained, whereas stress is partly released at the domain walls. **d**, **e**, HAADF-STEM (**d**) and bright-field TEM (**e**) images of $TbMnO_3$ thin films with the same thickness in plane-view configuration, showing a coincident in-plane domain structure.

this model, a simple domain wall structure can be proposed on the basis of the alternation of fully Tb-occupied columns ('Tb columns') and Tb-deficient columns ('X columns') of A sites of the ABO_3 perovskite structure, which could be attributed either to Tb vacancies or to replacement of Tb by a lighter element. Though HAADF imaging suggests the exis-

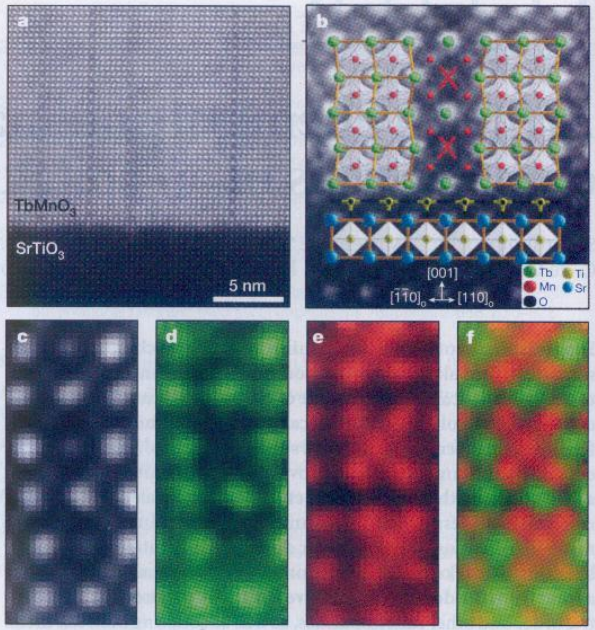

Figure 2 | Structure and chemistry of the domain walls. **a**, HAADF-STEM image of the $TbMnO_3$–$SrTiO_3$ interface. **b**, Detail of a domain wall close to the interface with the substrate, with the proposed atomic model superimposed. **c**–**f**, Spectrum image of the domain wall collected simultaneously with the HAADF signal (**c**): integrated intensities of the Tb $M_{4,5}$ (**d**) and Mn $L_{2,3}$ (**e**) edges from the spectrum image. **f**, Colour map composed using **d** and **e**, with the Mn signal in red and the Tb signal in green, showing the substitution of alternate Tb atoms for Mn to create a new 2D phase at the domain wall.

so distinct from that of the bulk material: strain-induced spin canting[18]

Эпитаксиальный синтез двумерной ферромагнитной фазы манганита тербия $TbMnO_3$ со структурой перовскита на поверхности титаната стронция $SrTiO_3$. В ходе эпитаксиального роста тонкой пленки антиферромагнитного $TbMnO_3$ в ней возникают механические напряжения, приводящие к стабилизации на границе между доменами экзотической двумерной кристаллической фазы. В результате перестройки структуры у антиферромагнетика, не обладающего намагниченностью, появляется постоянная намагниченность.

S. Farokhipoor, et. al. Artificial chemical and magnetic structure at the domain walls of an epitaxial oxide. Nature. 2014. v. 515. 379-383.

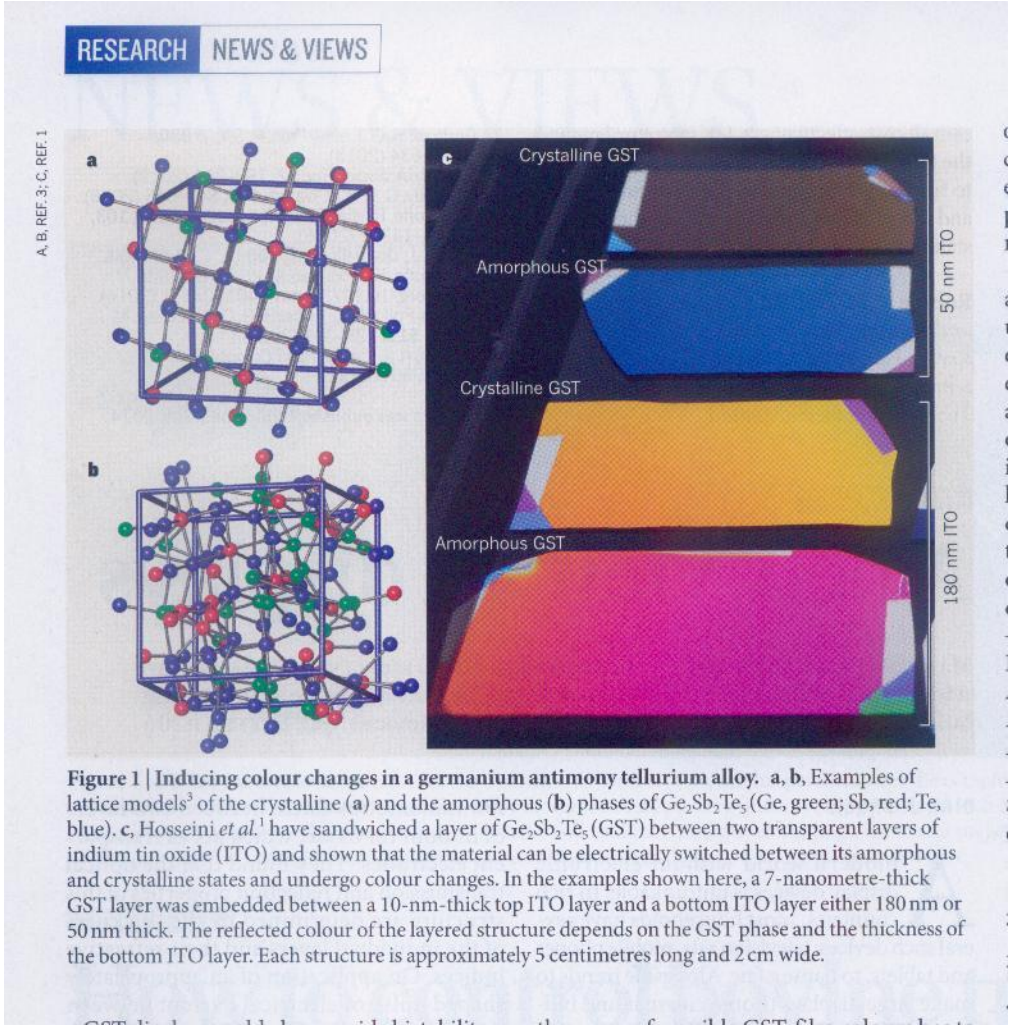

Figure 1 | Inducing colour changes in a germanium antimony tellurium alloy. **a**, **b**, Examples of lattice models[3] of the crystalline (**a**) and the amorphous (**b**) phases of $Ge_2Sb_2Te_5$ (Ge, green; Sb, red; Te, blue). **c**, Hosseini *et al.*[1] have sandwiched a layer of $Ge_2Sb_2Te_5$ (GST) between two transparent layers of indium tin oxide (ITO) and shown that the material can be electrically switched between its amorphous and crystalline states and undergo colour changes. In the examples shown here, a 7-nanometre-thick GST layer was embedded between a 10-nm-thick top ITO layer and a bottom ITO layer either 180 nm or 50 nm thick. The reflected colour of the layered structure depends on the GST phase and the thickness of the bottom ITO layer. Each structure is approximately 5 centimetres long and 2 cm wide.

Обратимый переход некоторых веществ из кристаллического а аморфное может быть вызвано внешним воздействием: теплом, светом, электрическим напряжением. Такие вещества могут служить, например, устройствами записи информации.

Электрически стимулированное изменение цвета $Ge_2Sb_2Te_5$ сплава. Структура монокристаллического (a) и аморфного (b) сплава (Ge -зеленый, Sb - красный, Te - синий) . Слой сплава находится между двумя прозрачными слоями окисла индия и олова. Цвет на отражение зависит от толщины и состояния сплава, а также от толщины нижнего слоя окисла индия и олова. На рисунке приведен случай для толщины слоя сплава 7 нм, верхнего слоя окисла индия и олова 10 нм и двух толщин (180 и 50 нм) нижнего окисла индия и олова. Размер пластин примерно 5x2 см.

P.Hosseini, et. al. Nature. 2014. 511. 206-211.

Двумерные кристаллы обладают физическими свойствами, отличными от объемных:

1. Пьезоэлектричество у молибденита, из-за снижения симметрии.
2. Остаточная намагниченность у антиферромагнетика манганита тербия $TbMnO_3$, из-за искажения структуры на границах доменов.
3. Непроницаемость тонких слоев нитрида бора, графена, молибденита для всех атомов; обусловлено высокой электронной плотностью между ядрами.
   Нитрид бора, графен – проницаемы для протонов, использование в атомной промышленности.
   (Rohit N. Karnik. Breakthrough for protons. Nature. 2014. 516. 173-175)
4. Двумерный карбид титана – перспективный накопитель электрической энергии.
   (M.Ghidiu et. al. Nature. 2014. 516. 78-81)

Непроницаемость тонких слоев нитрида бора, графена, молибденита для всех атомов; обусловлено высокой электронной плотностью между ядрами.

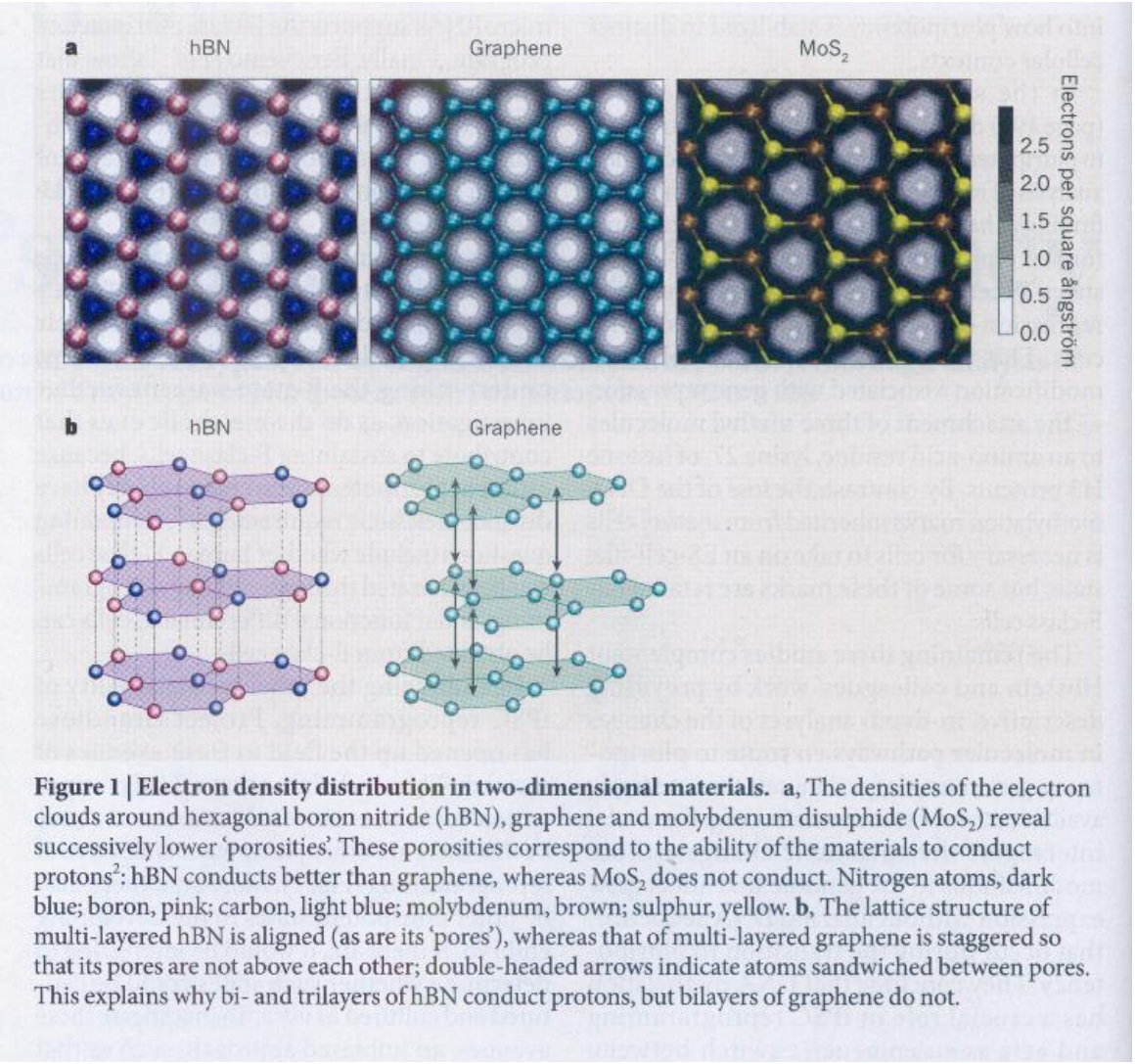

Figure 1 | Electron density distribution in two-dimensional materials. **a**, The densities of the electron clouds around hexagonal boron nitride (hBN), graphene and molybdenum disulphide (MoS_2) reveal successively lower 'porosities'. These porosities correspond to the ability of the materials to conduct protons[2]: hBN conducts better than graphene, whereas MoS_2 does not conduct. Nitrogen atoms, dark blue; boron, pink; carbon, light blue; molybdenum, brown; sulphur, yellow. **b**, The lattice structure of multi-layered hBN is aligned (as are its 'pores'), whereas that of multi-layered graphene is staggered so that its pores are not above each other; double-headed arrows indicate atoms sandwiched between pores. This explains why bi- and trilayers of hBN conduct protons, but bilayers of graphene do not.